

Hydrodynamics of larval fish quick turning: A computational study

Jialei Song^{1,2}, Yong Zhong², Haoxiang Luo³, Yang Ding¹ and Ruxu Du²

Proc IMechE Part C:
J Mechanical Engineering Science
2018, Vol. 232(14) 2515–2523
© IMechE 2017
Reprints and permissions:
sagepub.co.uk/journalsPermissions.nav
DOI: 10.1177/0954406217743271
journals.sagepub.com/home/pic



Abstract

A three-dimensional fluid–body interaction model was established to study the hydrodynamics of larval fish at a quick start with a turning angle of approximately 80° . The bending curves of the larval fish were attained by extracting the middle line of fish snapshots from a previously published paper. The fluid–body interaction was implemented to empower the self-propelling function of the larval fish. In this study, the swimmer’s kinematics of the body as well as hydrodynamics at preparatory and propulsive stages of the larval fish were extensively analysed. It shows that during the preparatory stage, the larval fish produces a significant force against the escaping direction. Nevertheless, this force leads to a large turning torque, helping to accomplish a quick turning. During the propulsive stage, the force increases quickly in the escape direction, resulting in a large velocity for the escape. The characteristics of body motion and the flow field are consistent with the previous observation on adult fish: the bimodal mode on velocity and tangential acceleration and three jets of fluids. In addition, the research also reveals that the forces generated at anterior and posterior parts of the larval fish generally point to the opposite directions at both preparatory and propulsive strokes of C-start.

Keywords

Quick start, turning, larval fish, hydrodynamics, computational fluid dynamics

Date received: 30 March 2017; accepted: 18 October 2017

Introduction

Through millions of years of evolution, fish have developed astonishing capabilities on swimming for locomotion.¹ These capabilities are crucial for the fish survival as they strongly affect foraging, reproduction and escaping from dangerous circumstances. Quick turn is one of the greatly important capabilities for fish to escape from predators and/or to catch preys. It has been shown that during quick turn, which lasts only a fraction of a second, the adult fish can reach a maximum speed of 10 body length per second (BL/s) and a maximum acceleration of more than 150 m/s^2 .^{2–4} Quick turning kinematics were classified into two types: C-start and S-start, which describe the shape that the fish bend into at the end of the first muscular contraction.^{5–8} The quick turn procedure is divided into three kinematic stages: the preparatory stroke, the propulsive stroke and a variable stage. During the preparatory stroke, one side of the body muscle contracts tightly to form a ‘C’ or an ‘S’ shape; during the propulsive stroke, the tail quickly flips back, resulting in a high forward acceleration; during the third stroke, varied types of motions might be executed, such as continuous swimming or coasting. Experimental measurements with

digital particle image velocimetry (DPIV) have shown that the flow field is featured by a vortex pair, forming a local jet flow directed to the opposite direction of the body bursting.⁹ Thus, the agility of fish quick turning is explained by the rapid generation of a vortex pair through body flexing and tail manipulation and by the absence of a separation drag.¹⁰ Tytell and Lauder¹¹ conducted an experimental study on the hydrodynamics of the escape response in bluegill sunfish using DPIV. They revealed that the escape response produced three distinct jets of fluids. Later, this observation was confirmed by Borazjani et al.¹² in an experiment-guided high-fidelity

¹Division of Mechanics, Beijing Computational Science Research Center, Beijing, China

²Department of Mechanical and Automation Engineering, The Chinese University of Hong Kong, Shatin, Hong Kong

³Department of Mechanical Engineering, Vanderbilt University, Nashville, USA

Corresponding author:

Yang Ding, Beijing Computational Science Research Center Building 9, East Zone, ZPark II, No. 10 Xibeiwang East Road, Beijing 100193, China.

Email: dingyang@csrc.ac.cn

numerical study. Using this study of the integrative sunfish as a control case, Borazjani^{13,14} further studied the hydrodynamic function roles of the anal/dorsal fins, as well as the caudal fin during fast C-starts by removing or erecting these fins. The research revealed that the effect of anal/dorsal fins was trivial on the instantaneous force production while the caudal fin generated a considerable hydrodynamic force, especially at the propulsive stroke stage.

Larval fish, like adult fish, undulate their bodies to generate propulsive force. Nevertheless, the propulsion mechanism is not necessarily the same as the adults' case due to differences in size, body stiffness and beat frequency, which lead to the low Reynolds number flow regime of the larval fish. In recent years, great progress has been made to understand the swimming of larval fish from different perspectives, such as morphology, kinematics and hydrodynamics. For example, Müller and van Leeuwen¹⁵ systematically studied the kinematics of larval zebrafish at age ranging from 2 to 21 days and presented the locomotion performance at periodical swimming, slow start and fast turn. The comparison of flow fields between the larval and the adult fish in a burst-and-coast mode was also done using DPIV but showed no qualitative differences.¹⁶ Several computational efforts were also made to understand the hydrodynamics of the quick start of larval fish. Combining flow simulations with an evolutionary optimisation algorithm, Gazzola et al.¹⁷ revealed that the optimised C-start motion is in good agreement with the observed kinematics; moreover, motion with a larger curvature might result in a larger escape distance. By collaborating with biologists, Li et al.¹⁸ reconstructed the high fidelity motion using morphological and kinematics data from real larval fish. They revealed that the thrust is mainly produced in the posterior half of the body. They also confirmed the observation of Gazzola et al.: increasing body wave amplitude results in the increase of forward swimming speed.

Even though many studies have been done using both experimental and computational methods, on larval fish quick start, many questions are still not well answered. For example, previous numerical studies on the quick start usually focus on the small turning angles ($\sim 30^\circ$). In practice, a large turning angle is usually adopted by fish for escape. More importantly, most of the research focused on the force production, flow field, power and locomotion efficiency of larval fish, and few studies emphasise the torque on the body that causes the turning and muscle actuation related to the hydrodynamics. This study aims to use the computational fluid dynamics to simulate the hydrodynamics of larval fish and then attentively focus on the dynamics and the actuation of the larva's body by quantifying the inertial and hydrodynamic torque. The rest of the paper is organised as follows. 'Materials and methods' section describes the materials and methods used in the modelling. 'Simulation

results and analysis' section gives the simulation results. Finally, 'Conclusions' section contains conclusions.

Materials and methods

Kinematics model reconstruction

The larval fish geometry used in this paper is similar to the simplified model of a larval zebrafish described in the study by Gazzola et al.¹⁷ This model assumes that the body's cross-section is elliptical with two orthogonal axis lengths $h(l)$ and $w(l)$, where l denotes the distance from the interested position to the tip of the snouts. The mathematical formulas of $h(l)$ and $w(l)$ are shown in Appendix 1. In the present study, the pectoral fins are not included, and we merely focus on the effect of the body. The curves of the larval fish midline come from the snapshots of a quick turning adult trout in the study by Harper and Blake.³ In that paper, several snapshots of a trout at fast start motion were presented. We digitised these images and obtained the centre lines of each posture. Then the centre line curves were incorporated with the geometry of a larval zebrafish to reconstruct the motion of the larval fish quick turning, as is shown in Figure 1. Please note that the study by Harper and Blake³ showed only the kinematics of the preparatory and propulsive stages, so we focused on these two stages

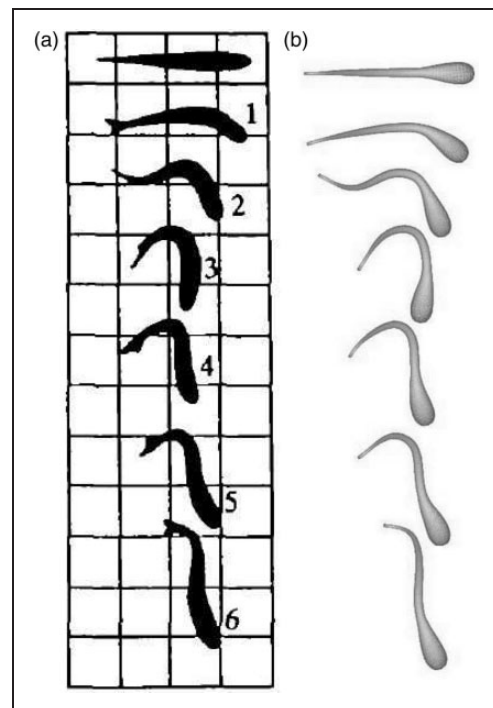


Figure 1. The original positions of a fish turning adapted from the study by Harper and Blake,³ and our reconstructed model is based on their midline curves and the larval fish geometry.

in the present paper. Temporal spline interpolation was used to generate the curves of the fish larva. Even though these curves come from different species and from an adult fish, it can still represent the kinematics of fish larva since the middle line curves are similar regardless of the species and age.^{15,16} Initially, the larval swimmer is set at the rest status. Then it swims freely without translational restrictions in the X and Y directions with the propulsion of contracting and stretching body laterally.

Simulation set-up

The water is assumed to be governed by the three-dimensional viscous incompressible continuity equation and the momentum equation

$$\nabla \cdot \mathbf{u} = 0 \quad (1)$$

$$\frac{\partial \mathbf{u}}{\partial t} + (\mathbf{u} \cdot \nabla) \mathbf{u} = -\frac{1}{\rho} \nabla p + \nu \Delta \mathbf{u} \quad (2)$$

where \mathbf{u} denotes the velocity vector, p denotes the pressure and ρ and ν denote the density and kinematic viscosity of water, respectively. The Navier–Stokes equations were solved by an in-house fluid solver, which implements the Ghost-cell immersed boundary method to treat the boundary. In this method, the fluid domain is discretised by non-uniform Cartesian mesh, and the ghost cell, whose nodes are inside the solid but have at least one neighbour in the fluid, is determined firstly. Then the image points in the fluid and the boundary intercept points are determined. Once they are determined, a trilinear interpolant is adopted to conform the pressure and velocity of the fluid to the force on the body surface. The stress σ on the surface is calculated according to the equation $\sigma_{i,j} = -p\delta_{i,j} + \frac{1}{2} \left(\frac{\partial v_i}{\partial x_j} + \frac{\partial v_j}{\partial x_i} \right)$, where $\delta_{i,j}$ is unit tensor and i,j is the integer sub-index from 1 to 3. The detail of this methodology is described by both Mittal et al.¹⁹ and Luo et al.²⁰ and Tian et al.²¹ Then force is calculated by $\mathbf{F} = \int_{\Omega} 1\sigma \cdot \mathbf{n} dS$, where \mathbf{n}

is surface normal and dS is the infinitesimal area on body surface area Ω . The background pressure, which is picked at the corner of the flow domain, is set as zero. Therefore, the integration of stress over the cross-section of the larval fish leads to zero on force. The fluid–body interaction is implemented using the explicit projection method.

A fixed, non-uniform, single-block Cartesian mesh is employed to discretise the fluid domain (Figure 2(a)). The size of the rectangular domain is $5L \times 5L \times 2L$, with a region near the larval fish body having the maximum resolution $1/250L$ in all three directions (L is the body length). Increasing the domain size by 1.5 times of the current size in each direction with the same resolution around the fish only leads to the maximum force difference of 1.31% in the Y direction, which means the current domain size is sufficient. The total number of Cartesian grid in the baseline simulation is 18 million ($410 \times 360 \times 120$). A coarser and a finer case with the finest resolution $1/200L$ and $1/300L$ were simulated for the mesh convergence study. The extra simulations produce a maximum of 4.6% and 4.0% difference, respectively, from the baseline mesh in the maximum force in the Y direction. An unstructured three-dimensional surface mesh was implemented to present the surface of the larval fish, as shown in Figure 2(b). The total node and element number are 2492 and 4980, respectively. A surface mesh of 50% finer gave the simulated force less than 4.2% difference in the Y direction. The Courant–Friedrichs–Lewy (CFL) condition number, which is defined as

$$CFL = \left(\frac{u}{\Delta x} + \frac{v}{\Delta y} + \frac{w}{\Delta z} \right) \Delta t \quad (3)$$

is less than 0.5 in the entire domain throughout the simulation, where u, v, w are the velocity components in the x, y, z directions, respectively, and $\delta x, \delta y, \delta z$ and δt are maximum spacial resolutions in the three orthogonal directions and time-marching resolution.

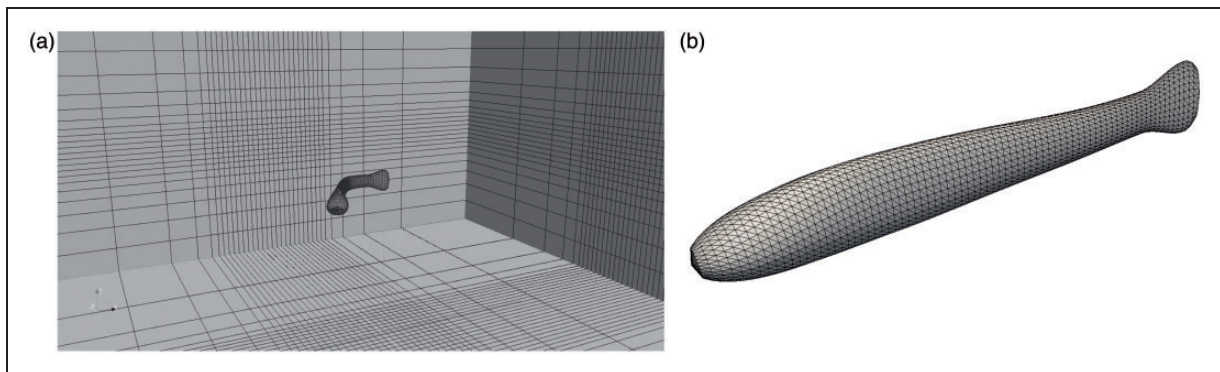


Figure 2. (a) The non-uniform Cartesian mesh around the larva (only 1 out of every 10 points in each direction is shown). (b) The unstructured triangular surface mesh of the larval fish body.

The MPI parallel computing was adopted in our in-house code. In the simulation, the flow field domain was decomposed into 40 subsections in the vertical direction with one core processing one subsection. Data communication happens at the touching interface of each subsection. Approximately 40 h were needed to complete the whole simulation. The characteristic velocity is defined as $U = L/T$, where T is the duration of the simulation, from the static status to approximately the end of propulsive stroke, when the position is shown in snapshot 6 in Figure 1(a). The Reynolds number defined by the characteristic velocity U and L is 100, which is within the range of real fish larva, ranging from 50 to 900 for cyclic swimming and slow start.¹⁵ Typically, only order of magnitude differences in Re are informative except at certain critical points like transition point from laminar to turbulence flow. The CFD code has been validated extensively in the previous work studying the complex moving boundaries' problems.^{22–24}

Simulation results and analysis

In the present work, we use the normalised values to describe the results. The translational acceleration is normalised as $a^* = aT^2/L$ and the translational velocity $V^* = VT/L$. The normalisation of other parameters will be described when they are used.

Kinematics

The postures of the larval fish in the quick start process is shown in Figure 3. In this figure, the colour

on the body surface presents the velocity distribution in the lab coordinate system $OXYZ$, with X axis being the initial direction of the larval fish, Y axis being the lateral orthogonal direction and Z being the upward direction. The velocity is the summation of the undulating velocity with respect to the body's centre of mass and the velocity of the centre of mass. From the figure, we can see that the posterior part of larval fish has a large velocity, which indicates a large force. The plot of the velocity amplitude, V^* , and tangential acceleration (defined as the first-order derivative of the velocity amplitude with respect to time), a^* , of the body's centre of mass, are shown in Figure 4(a). Scaling of the velocity and acceleration using the parameters of a two-day larval zebrafish ($\rho = 1000 \text{ kg/m}^3$ and $\nu = 1.004 \times 10^{-6} \text{ m}^2/\text{s}$), the maximum velocity and the acceleration are 67 BL/s and 124.4 m/s^2 , respectively, which are comparable to the measured value by Müller et al.¹⁵ In their paper, the maximum velocity and acceleration are 60 BL/s and 133 m/s^2 , respectively. A remarkable feature of the motion is the tangential deceleration at $t/T = 0.4 - 0.6$, which approximately corresponds to the time when the larval fish transits from position 5 to position 8 in Figure 3.

Figure 4(a) shows the translational velocity and tangential acceleration of the larval fish. Both the velocity and acceleration experience significant declinations around $t/T = 0.5$, forming a bimodal pattern. Such biomodal pattern was consistent with the previous observations on adult trout and pike fish.^{3,25} The larval fish body is deformed during the quick turn. In order to calculate the rotation of the

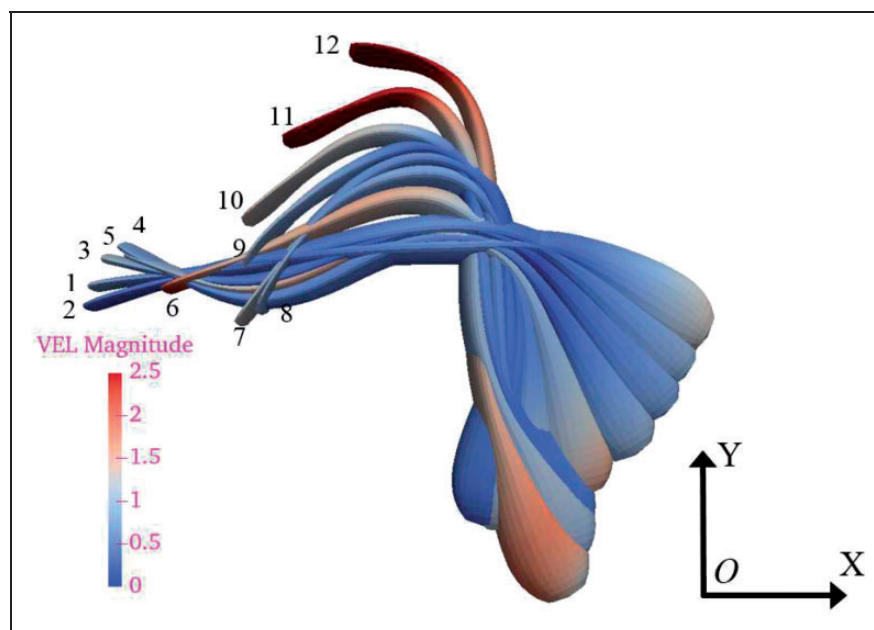


Figure 3. The computed larval fish positions and the velocity magnitude distribution on the body surface during quick turning. Position 1 corresponds to snapshot 1 and position 12 corresponds to snapshot 6 in Figure 1. Other positions are plotted with the same time interval.

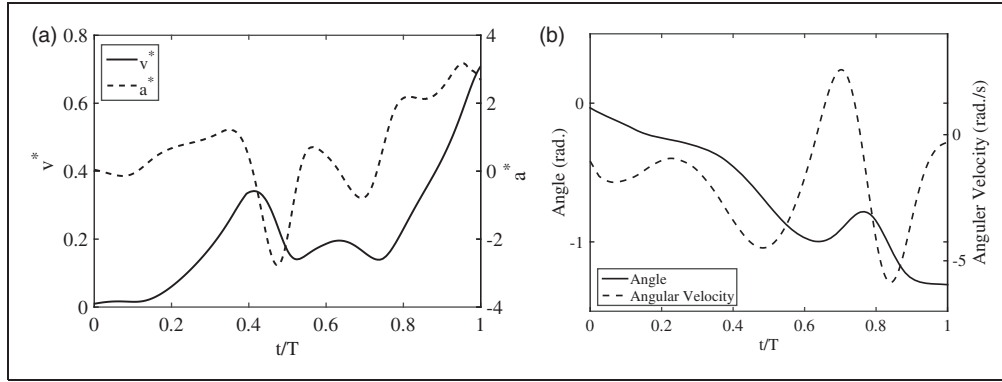


Figure 4. Translational velocity magnitude and tangential acceleration (a) and the rotational quantities (b) during the fast turning of the larval fish.

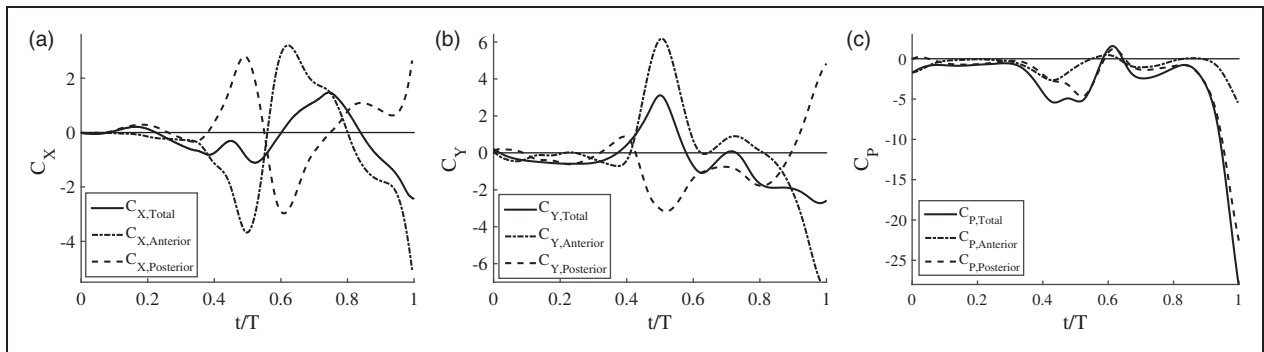


Figure 5. Hydrodynamic parameters of the larval fish quick turning: force coefficient in X (a) and Y (b) directions and hydrodynamic power output of the entire body, the anterior half and the posterior half (c).

deformable fish, we define the rotation angle $\theta = \frac{\sum I_i \theta_i}{\sum I_i} = \frac{\sum I_i \theta_i}{I_0}$, where $\theta_i = \arctan \frac{v_i - v_{CoM}}{x_i - x_{CoM}}$ represents the angle of an infinitesimal segment about the centre of mass. Figure 4(b) refers to the yaw rotation angle θ and angular velocity $\dot{\theta}$ of the larval fish. Initially, the larval fish aligns in the X direction and θ is zero, then θ consecutively decreases to -1.37 rad. During $t/T = 0.4 - 0.6$, the fish exhibits a large angular velocity $\dot{\theta}$. At $t/T = 0.7$ and 0.8 , $\dot{\theta}$ is also at the extreme value, which is due to the rotation of the anterior part. Please note that the deceleration of the centre of mass coincides with the rotation at $t/T = 0.4 - 0.6$, which will be discussed in the later section.

Force and power

The force components, F_X , F_Y and F_Z , are normalised by the fluid density ρ , the maximum area of cross-section perpendicular to the body’s long axis $S = 0.012L^2$ and the characteristic velocity U , according to

$$C_X = \frac{F_X}{0.5\rho U^2 S}, \quad C_Y = \frac{F_Y}{0.5\rho U^2 S}, \quad C_Z = \frac{F_Z}{0.5\rho U^2 S} \quad (4)$$

where C_X , C_Y and C_Z are force coefficients. Since the morphology of larval fish model is symmetric with respect to the horizontal middle plane, the forces in the vertical directions cancel out, so C_Z and F_Z of the entire body are zero. In order to find out the role of the head and tail during the quick turn, the whole body is divided into anterior and posterior parts at $l/L = 0.57$, where the curvature is largest at time $t/T = 0.5$. Figure 5(a) and (b) show the time courses of the force coefficients in X and Y directions, respectively. The most remarkable feature is that these two forces increase significantly in amplitude around $t/T = 0.4 - 0.6$, reaching 1.6 in the X direction and 2.4 in the Y direction in absolute value but the resultant force pointing to the opposite direction of the escaping. This duration is correspondent to the deceleration in Figure 4(b). Before these sharp increases, the forces both in X and Y directions change slowly. After $t/T = 0.6$, C_Y changes back to the escaping directions and the magnitude increases sharply and reaches 2.6; in comparison, the change of C_X is smaller, ranging within 1.5 until the end of the simulated time. The anterior and posterior parts of the body generally produce the opposite force in the X direction, leading to a small C_X during the entire duration. In the Y direction, the anterior and posterior parts also produce opposite

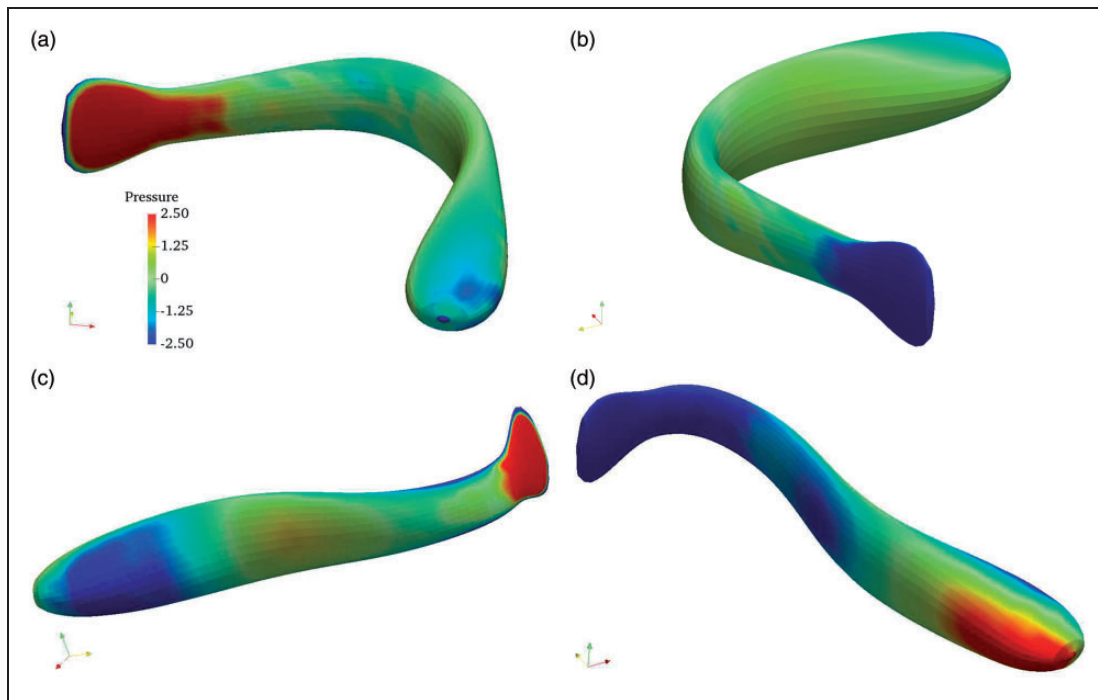


Figure 6. Pressure p^* distribution on the larval fish surface at time $t/T = 0.5$ (a, b) and $t/T = 0.9$ (c, d).

forces. Under similar kinematics, Borazjani simulated the adult sunfish and presented the force production during the entire duration.¹² The result shows that the forces in the initial oriented direction and escaping direction share a similar force magnitude, which is consistent with the present observation. Figure 6 shows the pressure $p^* = p/(0.5\rho U^2)$ distribution on the larval fish body surface at two typical times at the preparatory stage $t/T = 0.5$ and the propulsive stage $t/T = 0.9$. At both time points, the posterior part dominates the force production. At $t/T = 0.5$, the concave side experiences the high pressure while the convex side experiences the low pressure. At $t/T = 0.9$, on the posterior part, the pushing part generates a large high pressure region while the lee side generates a very low pressure region.

The hydrodynamic power is calculated by the integration on the larval fish body surface of the dot product of force and the velocity: $P = \int_{\Omega} \mathbf{f} \cdot \mathbf{u} \, dS$, where \mathbf{f} and \mathbf{u} are the force and velocity on the body surface, respectively. Moreover, the power coefficient is defined as $C_p = P/(0.5\rho U^3 S)$. The time course of power coefficient is shown in Figure 5(c). In this figure, the positive power indicates that the larval fish attains energy from the surrounding fluid, whilst the negative power indicates that the larval fish needs to consume energy to propel itself. In the period $t/T = 0.3 - 0.6$, a considerable amount of power, with the peak value 5.4, is consumed by the larval fish for propulsion. Then after $t/T = 0.6$, at the propulsive stage, the output power increases sharply to approximately 30. During the body contraction period $t/T = 0.4 - 0.6$ (corresponding to Position 5

to Position 8 in Figure 3), both parts consume power. This indicates that the wake body interaction is not significant during the quick turning. The anterior and posterior parts need power to conquer the fluid drag to turn the head quickly to the escaping direction, and to form the 'C' curve. After $t/T = 0.86$, in the propulsive stage, most power is consumed on the posterior part, taking about 84% of the total power consumption.

Vortex dynamics

As a larval fish swims, vortices are formed as the 'footprints', which leave the messages on the swimming hydrodynamics. The vorticity in the vertical direction is $\omega_z = \frac{\partial u}{\partial y} - \frac{\partial v}{\partial x}$, where u and v are the fluid velocity components in X and Y directions, respectively. The normalised vorticity is scaled as $\omega_z^* = \omega_z T$. The flow field at preparatory stroke $t/T = 0.6$ and propulsive stroke $t/T = 0.9$, are shown in Figure 7. At preparatory stroke, a strong clockwise vortex TV1 continuously forms and sheds at the end of the preparatory stage (Figure 7(a)), which is consistent with the DPIV measurement and simulation of bluegill sunfish.¹² However, at the propulsive stroke, the burst of tail induces the large anticlockwise vortex TV2 (Figure 7(b)), which is similar to the simulation results on the C-start of a larva model at the escaping turning angle is less than 30° ¹⁷ as well as the vortex observation from Tytell and Lauder¹¹ and Borazjani et al.¹² Meanwhile, three jets of fluids are observed in the present study, with Jet 1 induced at the tail, Jet 2 induced at the middle part and Jet 3 at the anterior

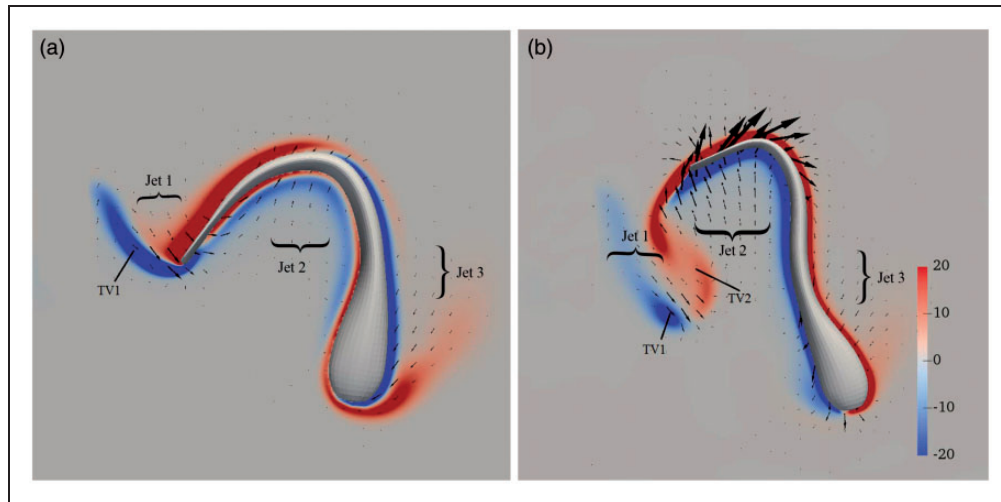


Figure 7. The vorticity ω_z^* in XY plane cutting the larval fish's middle body at preparatory stage $t/T = 0.6$ (a) and at propulsive stage $t/T = 0.9$ (b).

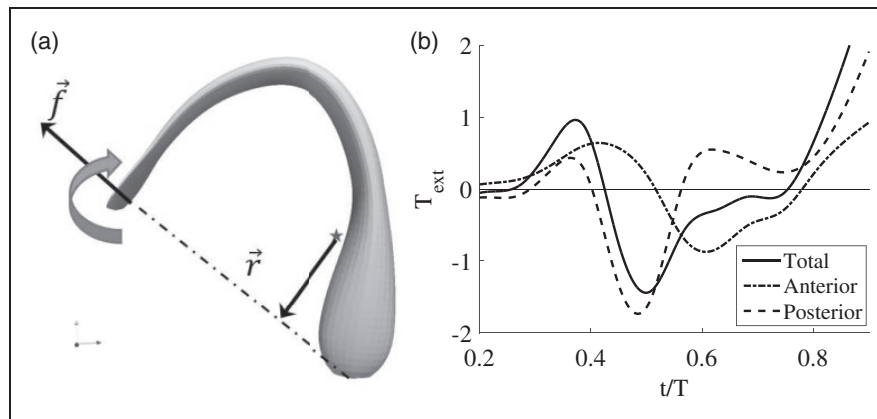


Figure 8. Illustration of the role of the tail force on the torque generation at preparatory stroke (a) and (b) time courses of torque generated by the entire body, the anterior and the posterior part.

part at preparatory stage; Jet 2 is strengthened by the tail at propulsive stage, which is consistent with the observation in Borazjani's study.¹² Please note that TV1 and TV2 are not merged together but remains a obvious vortex pair, a characterised fluid structure that was observed before.^{9,10} This observation also shows that the wake capture mechanism, which is commonly used on insect flight, is not significant at the larval fish quick turning.

External torque

Intuitively, whatever the fish intends to capture a prey or escape from a dangerous circumstance, quick acceleration and fast movement are greatly favoured to reduce the time for moving the intended distance. However, many fish decelerate during the quick start and turn case.^{3,25} Why do the fish undertake this process? A simple model was proposed to answer this question. Figure 8(a) shows the situation

at $t/T = 0.5$, when a considerable deceleration takes place. From the pressure distribution in Figure 6(a) and (b), the large pressure is generated at the tail, and the force directs to opposite to the escaping direction. The torque is calculated based on the mathematical formula $\mathbf{T} = \int_{\Omega} \mathbf{r}' \times \mathbf{f} \, dS$, where \mathbf{r}' is the position vector with respect to the instantaneous centre of mass. Under this definition, $\frac{d}{dx}(\Sigma \mathbf{r}'_i \times m_i \mathbf{v}_i) = \Sigma \mathbf{r}'_i \times \mathbf{F}_i^{ext}$ is satisfied, where \mathbf{v}_i and \mathbf{F}_i^{ext} are the velocity and hydrodynamic force in laboratory coordinate system, respectively. We found that the resultant torque on tail is in the clockwise direction (Figure 8(b)). This indicates that it is the tail force that causes the deceleration, drives the yaw turning of the body to the escaping direction. The time courses of external torque generated on anterior and posterior parts are also shown in Figure 8(b). A large clockwise torque (negative value in the plot) is observed around the time $t/T = 0.5$ on the tail. For the real and untouched larval fish, the flapping

of pectoral fins during quick turning is observed,¹⁵ which can potentially contribute to torque for turning. However, since pectoral fins' surface area is so small compared with the tail area, their contribution is also much smaller than the tail contribution.

Conclusions

In this paper, we used a fluid–body interaction model to study the hydrodynamics of quick turning of the larval fish. According to the discussions above, the following conclusions can be drawn: (a) The simulation results reveal a clear bimodal pattern on the displacement, velocity and acceleration that are consistent with the observations reported in the previous literature. (b) The larval fish quick turn is decomposed into two stages: the preparatory stage and the propulsive stage. In the preparatory stage, in order to generate a large external torque to achieve the turning, a large force opposite to the escaping direction is generated on the tail. This would sacrifice the velocity to achieve the quick turning. (c) The roles of the anterior and posterior parts of the body are scrutinised, showing that the anterior and posterior parts generally produce the forces in opposite directions, but both parts consume the power. (d) During the transition from preparatory stroke to propulsive stroke, the posterior part plays the dominant role in turning while the anterior part acts as a resistive factor. (e) Qualitatively, the observations on motion, flow fields as well as the muscle wave propagation of larval fish are all similar to the adult fish. It should be noted that since the larval fish's dorsal fin, anal fin as well as pectoral fins have not fully developed, they play a marginal role on the force production due to the small fin surface area. For adult fishes, though, the results could be significantly different.^{11,12,25} As to the anal/dorsal fins of adult fish, an in-depth study of Borazjani¹³ using experimentally guided numerical simulations revealed that during preparatory and propulsive strokes of C-start, these fins contribute less than 5% of the instantaneous force. Meanwhile, significant pectoral fins' extension during escapes was observed on adult marble hatchetfish (*Carnegiella strigata*)²⁶ and adult knife fish (*Xenomystus nigri*),²⁷ and the orientation of pectoral fins may contribute to displacement in the vertical plane. In the future, we will consider the effects on these fins and quantitatively study their roles on the quick turning and compare the differences between the adult fish with the larval fish.

Acknowledgement

The authors acknowledge Journal of Experimental Biology for granting the permission to duplicate Figure 1(a) in the paper.

Declaration of Conflicting Interests

The author(s) declared no potential conflicts of interest with respect to the research, authorship, and/or publication of this article.

Funding

The author(s) disclosed receipt of the following financial support for the research, authorship, and/or publication of this article: This project was partially funded by the CUHK grant no. C4022-14G to R Du and J Song and partially funded by the NSFC grant no. 11672029, NSAF-NSFC grant no. U1530401 to Y Ding. The computational resources were provided by the National Supercomputer Center (Guangzhou) and CSRC.

References

1. Fish FE and Lauder GV. Passive and active flow control by swimming fishes and mammals. *Annu Rev Fluid Mech* 2006; 38: 193–224.
2. Webb PW. Effects of median-fin amputation on fast-start performance of rainbow trout (*Salmo gairdneri*). *J Exp Biol* 1977; 68: 123–135.
3. Harper DG and Blake RW. Fast-start performance of rainbow trout *salmo gairdneri* and northern pike *esox lucius*. *J Exp Biol* 1990; 150: 321–342.
4. Frith HR and Blake RW. Mechanics of the startle response in the northern pike, *Esox lucius*. *Can J Zool* 1991; 69: 2831–2839.
5. Webb PW. Fast-start performance and body form in seven species of teleost fish. *J Exp Biol* 1978; 74: 211–226.
6. Jayne BC and Lauder GV. Red and white muscle activity and kinematics of the escape response of the bluegill sunfish during swimming. *J Comp Physiol A* 1993; 173: 495–508.
7. Domenici P and Blake RW. The kinematics and performance of the escape response in the angelfish (*Pterophyllum eimekei*). *J Exp Biol* 1991; 156: 187–205.
8. Domenici P and Blake R. The kinematics and performance of fish fast-start swimming. *J Exp Biol* 1997; 200: 1165–1178.
9. Wolfgang MJ, Triantafyllou MS and Yue DKP. Visualization of complex near-body transport processes in flexible-body propulsion. *J Visual* 1999; 2: 143–151.
10. Triantafyllou MS, Triantafyllou GS and Yue DKP. Hydrodynamics of fishlike swimming. *Annu Rev Fluid Mech* 2000; 32: 33–53.
11. Tytell ED and Lauder GV. Hydrodynamics of the escape response in bluegill sunfish, *Lepomis macrochirus*. *J Exp Biol* 2008; 211: 3359–3369.
12. Borazjani I, Sotiropoulos F, Tytell ED, et al. Hydrodynamics of the bluegill sunfish c-start escape response: three-dimensional simulations and comparison with experimental data. *J Exp Biol* 2012; 215: 671–684.
13. Borazjani I. The functional role of caudal and anal/dorsal fins during the c-start of a bluegill sunfish. *J Exp Biol* 2013; 216: 1658–1669.
14. Borazjani I. Simulations of unsteady aquatic locomotion: from unsteadiness in straight-line swimming to fast-starts. *Integr Comp Biol* 2015; 55: 740–752.
15. Müller UK and van Leeuwen JL. Swimming of larval zebrafish: ontogeny of body waves and implications for locomotory development. *J Exp Biol* 2004; 207: 853–868.
16. Muller UK, Stamhuis EJ and Videler JJ. Hydrodynamics of unsteady fish swimming and the

- effects of body size: comparing the flow fields of fish larvae and adults. *J Exp Biol* 2000; 203: 193–206.
17. Gazzola M, Van Rees WM and Koumoutsakos P. C-start: optimal start of larval fish. *J Fluid Mech* 2012; 698: 5–18.
 18. Li G, Müller UK, van Leeuwen JL, et al. Body dynamics and hydrodynamics of swimming fish larvae: a computational study. *J Exp Biol* 215: 4015–4033.
 19. Mittal R, Dong H, Bozkurtas M, et al. A versatile sharp interface immersed boundary method for incompressible flows with complex boundaries. *J Comput Phys* 2008; 227: 4825–4852.
 20. Luo H, Dai H, de Sousa PF, et al. On the numerical oscillation of the direct-forcing immersed-boundary method for moving boundaries. *Comput Fluid* 2012; 56: 61–76.
 21. Tian F-B, Dai H, Luo H, et al. Fluid–structure interaction involving large deformations: 3D simulations and applications to biological systems. *J Comput Phys* 2014; 258: 451–469.
 22. Dai H, Luo H and Doyle JF. Dynamic pitching of an elastic rectangular wing in hovering motion. *J Fluid Mech* 2012; 693: 473.
 23. Song J, Luo H and Hedrick TL. Three-dimensional flow and lift characteristics of a hovering ruby-throated hummingbird. *J Royal Soc Interface* 2014; 11: 20140541.
 24. Song J, Tobalske BW, Powers DR, et al. Three-dimensional simulation for fast forward flight of a calliope hummingbird. *Open Sci* 2016; 3: 160230.
 25. Harper DG and Blake RW. Prey capture and the fast-start performance of northern pike *Esox lucius*. *J Exp Biol* 1991; 155: 175–192.
 26. Eaton RC, Bombardieri RA and Meyer DL. The Mauthner-initiated startle response in teleost fish. *J Exp Biol* 1977; 66: 65–81.
 27. Kasapi MA, Domenici P, Blake RW, et al. The kinematics and performance of escape responses of the knifefish *Xenomystus nigri*. *Can J Zool* 1993; 71: 189–195.

and width $w(l)$. The half width of the elliptical section $w(l)$ is defined as

$$w(l) = \begin{cases} w_h \sqrt{1 - \left(\frac{l-l_b}{l_b}\right)^2}, & 0 \leq l < l_b \\ (-2(w_t - w_h) - w_t(l_t - l_b)) \left(\frac{l-l_b}{l_t-l_b}\right)^2 \\ + (-3(w_t - w_h) + w_t(l_t - l_b)) & l_b \leq l < l_t \\ \times \left(\frac{l-l_b}{l_t-l_b}\right)^2 + w_h, \\ w_t - w_t \left(\frac{l-l_t}{L-l_t}\right)^2, & l_t \leq l < L \end{cases} \quad (5)$$

where L denotes the body length, $w_h = 0.0635L$, $w_t = 0.0254L$, $l_b = 0.0862L$, and $l_t = 0.3448L$. The semi-height of the elliptical section $h(l)$ is defined as

$$h(l) = \begin{cases} h_1 \sqrt{1 - \left(\frac{l-l_1}{l_1}\right)^2}, & 0 \leq l < l_1 \\ 2(h_2 - h_1) \left(\frac{l-l_1}{l_2-l_1}\right)^3 \\ + 3(h_2 - h_1) \left(\frac{l-l_1}{l_2-l_1}\right)^2 + h_1, & l_1 \leq l < l_2 \\ 2(h_3 - h_2) \left(\frac{l-l_2}{l_3-l_2}\right)^3 \\ + 3(h_3 - h_2) \left(\frac{l-l_2}{l_3-l_2}\right)^2 + h_2, & l_2 \leq l < l_3 \\ h_3 \sqrt{1 - \left(\frac{l-l_3}{L-l_3}\right)^2}, & l_3 \leq l < L \end{cases} \quad (6)$$

where L denotes the body length, $h_1 = 0.072L$, $h_2 = 0.041L$, $h_3 = 0.071L$, $l_1 = 0.284L$, $l_2 = 0.844L$, and $l_3 = 0.957L$.

Appendix I

This model adopted an assumption that the cross-section of the larva is elliptical with the height $h(l)$